New CaRbNaZ (Z=Si and Ge) semiconductor compounds suitable for photovoltaic and thermoelectric devices

A. Righi[a], F. Bendahma[a,*], A. Labdelli[b], M. Mana[c], R. Khenata[d] T. Seddik[d], G. Ugur[e], and W. Ahmed[f]

[a]*Laboratory of Technology and Solid Properties, Abdelhamid Ibn Badis University, 27000 Mostaganem, Algeria,*
[*]*e-mail: f.bendahma@yahoo.fr*
[b]*Biotechnology Applied to Agriculture and Environment Preservation Laboratory, Abdelhamid Ibn Badis University, 27000 Mostaganem, Algeria.*
[c]*Abdelhamid Ibn Badis University, 27000 Mostaganem, Algeria,*
[d]*Laboratoire de Physique Quantique de La Matière et de La Modélisation Mathématique, Université de Mascara, 29000, Mascara, Algeria,*
[e]*Department of Physics, Faculty of Science, Gazi University, 06500 Ankara, Turkey,*
[f]*UAE University, COE, Al Ain, UAE.*

Received 28 February 2024; accepted 5 September 2024

Semiconductor compounds are a fascinating type of materials that have attracted the attention of scientists because of their ability to enhance green technology by efficiently converting, storing, and transmitting waste heat into electrical energy. This research aimed to investigate the structural, electronic, elastic, optical, and thermoelectric characteristics of newly developed Quaternary Heusler alloys (QHAs) CaRbNaZ (where Z represents Si and Ge). This was achieved using the generalized gradient approximation (GGA) and the Tran-Blaha modified Becke-Johnson (TB-mBJ) potential. For both approximations, CaRbNaSi and CaRbNaGe are found to be nonmagnetic semiconductors with band gaps varying in the range from 0.49 to 1.00 eV. The studied alloys additionally conform to the Slater-Pauling rule, exhibiting a specific magnetic moment of $M_{\text{tot}} = 8 - Z_{\text{tot}}$ for nonmagnetic behavior and, therefore, having a total magnetic of 0.00 μ_B. They possess an optical band gap comparable to the electronic band gap, along with significant absorption properties (90×10^4 and 103×10^4 cm^{-1}) in visible and UV regions, respectively, proving that these compounds are promising materials for photovoltaic cells and UV radiation shields. The high merit factor values (0.76 and 0.80) at 300K confirm that CaRbNaZ (Z= Si and Ge) are suitable candidates for thermoelectric devices.

Keywords: Optical properties; absorption; photovoltaic cells; elastic constants; alternative green technology.

DOI: https://doi.org/10.31349/RevMexFis.71.011001

1. Introduction

Ultra-modern lifestyles, population growth, high fossil fuel prices, global warming, and pollution necessitate environmentally friendly solutions. These growing concerns about global energy have recently encouraged scientists to seek new thermoelectric (TE) semiconductor materials to meet the world's increasing energy needs. Thermoelectric devices are environmentally friendly, serving as a green power generation resource with advantages such as small size, high reliability, absence of pollutants, effective waste-heat recovery systems, and feasibility over a wide temperature range [1, 2].

The TE features of materials are evaluated through the mathematical model:

$$ZT = \frac{S^2 \sigma T}{K}. \tag{1}$$

Here, K, T, σ, and S represent the thermal conductivity, temperature, electrical conductivity, and Seebeck coefficient, respectively [3–5]. The optimal performance of thermoelectric materials is achieved when they exhibit low thermal conductivity, high electrical conductivity, and a high Seebeck coefficient. These requirements can be met in narrow band gap semiconductors capable of maximizing energy harvesting from the solar spectrum [6], such as Heusler alloys (HAs).

Heusler alloys have garnered significant attention as crucial technological solutions for addressing energy issues. These alloys exist in binary, ternary, quaternary, and multinary forms are well-suited as solar cells (SCs) for thermoelectric fields due to their high stability, good optical properties, and environmental friendliness at an affordable cost [7–9]. In this regard, SC efficiency may be enhanced by employing innovative HAs, such as Quaternary Heusler Alloys (QHAs), which exhibit high absorption and minimal photon energy inefficiencies, serving as a better alternative to commercial silicon-based solar cells. QHAs, with a chemical formula XX'YZ, possess a LiMgPdSn-type structure (or Y-type) along with the F43m (No. 216) space group [10]. Many studies of QHAs have been conducted, focusing on their half-metallic (HM), semiconducting (SC), semimetallic properties (SMP), and spin-gapless semiconductors (SGS) [11, 12]. Numerous studies have explored the half-metallicity, optical, and thermoelectric properties of various Quaternary Heusler compounds that obey the 18-electron rule as introduced by Jiangang He *et al*. [13], such as CoIrMnZ (Z=Al, Si, Ga, Ge) [14], YRhTiGe [15], FeRhCrSi, FePdCrSi [16], PdCoM-

nAl [17], CrTiRhAl [18], LiScPdPb [19], and ZnFeTiSi [20]. From the literature reviews, it can be concluded that d^0-based semiconducting quaternary Heusler compounds have been less investigated, particularly those with a valence electron count (VEC) equal to 8. Therefore, we are encouraged to apply ab-initio computations to analyze the electronic, thermoelectric, elastic, optical, and structural characteristics of new Quaternary Heusler alloys, specifically CaRbNaZ (Z= Si, Ge). The remaining portions of this article are organized as follows: Computation details, results and discussion, and a brief summary.

2. Computational details

Investigating thermoelectric, optical, lattice dynamics, and structural stability, including electronic properties of CaRbNaZ (Z=Si and Ge) compounds, the full potential linear augmented-plane waves (FP-LAPW) approach has been employed in the `Wien2k` software [21]. The exchange correlation function has been calculated using the GGA (generalized gradient approximation) following the PBE (Perdew-Burke-Ernzerhof) method [22]. Given that the GGA typically underestimates material band gaps, we used the Tran-Blaha modified Becke-Johnson (TB-mBJ) potential. This method is known for accurately determining band gaps in electronic structures and providing better analysis of optical properties [23–25]. Moreover, the mBJ approach yields theoretical results that are very similar to experimental data for energy gaps in semiconductors and insulators [26, 27].

Additionally, the mBJ potential is highly adaptable, precise, and easy to use [28]. In the calculations, the muffin-tin sphere radii were automatically set to 2.00 Bohr for Ca, Rb, and Na atoms, and 1.93 Bohr for Z atoms. The magnitude of the greatest vector magnitude is 12 (*i.e.*, $G_{\max}$) in charge density Fourier expansion. With a matrix size of RMT * Kmax set to 8, where $Kmax$ represents the plane wave cut-off, the partial waves within the atomic spheres are expanded up to $lmax = 10$. A k-mesh of $15 \times 15 \times 15$ was selected for SCF and band structure calculations. Additionally, the cut-off energy, set at -6 Ry, determines the separation between valence and core states. For successive iterations of self-consistent field (SCF) cycles, we set an energy convergence criterion of 10^{-5} Ry. A dense k-mesh of $50 \times 50 \times 50$ k-points was utilized to calculate optical parameters because optical spectra highly depend on Brillouin zone sampling. Using the semi-classical Boltzmann transport equation with rigid band and constant relaxation time approximations, the thermoelectric transport properties were determined [29].

3. Results and discussions

3.1. Structural properties

In general, each Heusler alloy can exhibit three distinct nonequivalent atomic configurations. Quaternary Heusler alloys (QHAs) possess a LiPdMgSb prototype structure and crystallize into face-centered cubic sublattices [30]:

Type I: Z(0,0,0), Na(1/4,1/4,1/4), Rb(1/2,1/2,1/2), and Ca(3/4,3/4,3/4).

Type II: Z(1/4,1/4,1/4), Na(1/2,1/2,1/2), Rb(0,0,0), and Ca(3/4,3/4,3/4).

Type III: Z(3/4,3/4,3/4), Na(1/4,1/4,1/4), Rb(1/2,1/2,1/2), and Ca(0,0,0).

Mainly unit cell of CaRbNaZ (Z = Si and Ge) Heusler alloys is shown in Fig 1. The alloys are non-magnetic (NM), as indicated by the calculations in the ferromagnetic phase, which show a total magnetic moment of zero. Figure 2 presents the estimated energy versus volume curve, which clearly indicates that the NM-type I state is more energetically stable than the type II and type III cases.

All structural parameters at equilibrium for the two compounds in different structure types are shown in Table I. Based on the equilibrium lattice constant results, the values are determined to be 7.73 and 7.81Å for CsRbNaSi and CsRbNaGe, respectively. Further confirmation of these results can be achieved by considering the atomic radii of Si

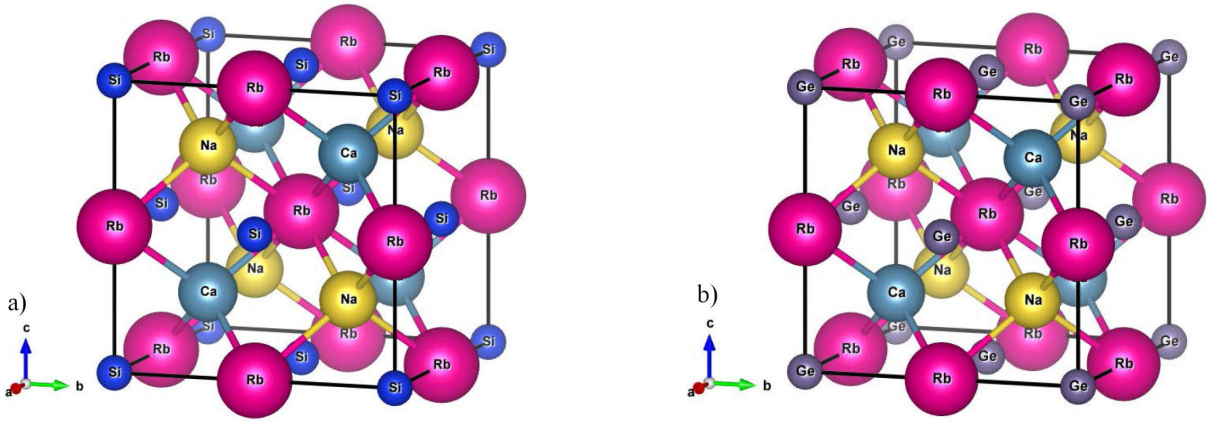

FIGURE 1. Crystal structure for CaRbNaSi and CaRbNaGe.

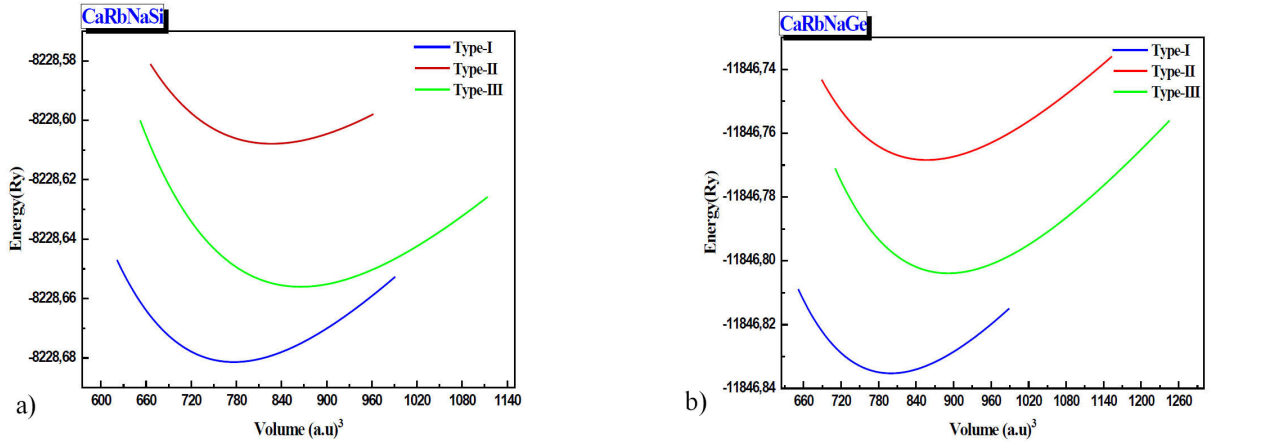

FIGURE 2. CaRbNaZ whole energy as a function of unit cell volume *i.e.*, (Z= Si and Ge).

TABLE I. The computed values of formation energy E_f, cohesive energy E_c, derivative of bulk modulus B', bulk modulus B, lattice constant a, and ground state energies E_0 for CaRbNaZ (Z= Si and Ge).

Alloys	Type	E_0 (Ry)		a (Å)	B (GPa)	B'	E_c (Ry)	E_f (Ry)
		FM	NM	NM	NM	NM	NM	NM
CaRbNaSi	Type I	-8228.6812	-8228.6812	7.72	21.96	4.28	-0.62	-0.58
	Type II	-8228.6087	-8228.6079	7.89	17.25	4.21	-	-
	Type III	-8228.6542	-8228.6560	8.01	19.28	4.16	-	-
CaRbNaGe	Type I	-11846.8352	-11846.8353	7.81	19.57	4.37	-0.59	-0.55
	Type II	-11846.7682	-11846.7682	7.98	15.51	4.19	-	-
	Type III	-11846.8025	-11846.8039	8.09	17.86	4.16	-	-

and Ge, which are 1.1 and 1.25 Å, respectively. In CaRbNaZ alloys, the atomic size of the Z element expands with the equilibrium lattice constant. Conversely, the bulk modulus B magnitudes diminish in the following order: B (CsRbNaSi) $> B$ (CsRbNaGe), in contrast to the lattice constant a, which follows the relationship $B \sim a^{-1}$ [31]. This pattern of variation in the different lattice parameters confirms the reliability and accuracy of our investigation.

To evaluate the bonding strength, cohesive energy Ec is utilized. It is defined as the difference between the total energy of the alloy and the sum of the energies of its individual atoms. The formula for cohesive energy per unit is expressed as below for CaRbNaZ (Z= Si and Ge) [32]:

$$E_{\mathrm{C}}^{\mathrm{CaRbNaZ}} = E_{\mathrm{tot}}^{\mathrm{CaRbNaZ}} - (E_{\mathrm{Ca}} + E_{\mathrm{Rb}} + E_{\mathrm{Na}} + E_{\mathrm{Z}}), \quad (2)$$

here $E_{\mathrm{C}}^{\mathrm{CaRbNaZ}}$ represents total energy at equilibrium conditions for CaRbNaZ, E_{Ca}, E_{Rb}, E_{Na} and E_{Z} (Z= Si and Ge) are the entire energies of the isolated atoms [33]. CaRbNaSi, having the lowest cohesive energy, is shown in Table I as the most stable structure. The negative values of E_c for all compounds ensure that these QHAs can be stabilized upon formation [34]. We have also calculated the formation energy E_f, which is typically employed to estimate whether the material in question can be experimentally fabricated. The preparation is energetically favorable, as indicated by the negative characteristic of this parameter, signifying an exothermic process. In general, E_f of CaRbNaZ (Z= Si and Ge) can be computed by implementing the following formula:

$$E_f^{\mathrm{CaRbNaZ}} = E_{\mathrm{tot}}^{\mathrm{CaRbNaZ}} - \left(E_{\mathrm{bulk}}^{\mathrm{Ca}} + E_{\mathrm{bulk}}^{\mathrm{Rb}} + E_{\mathrm{bulk}}^{\mathrm{Na}} + E_{\mathrm{bulk}}^{Z}\right). \quad (3)$$

Here, $E_{\mathrm{tot}}^{\mathrm{CaRbNaZ}}$ represents the total energy of the primitive cell of CaRbNaZ, and $E_{\mathrm{bulk}}^{\mathrm{Ca}}$, $E_{\mathrm{bulk}}^{\mathrm{Rb}}$, $E_{\mathrm{bulk}}^{\mathrm{Na}}$, and E_{bulk}^{Z} (Z = Si and Ge) are the full energies for both Si and Ge atoms in their bulk states. The feasibility of experimentally synthesizing CaRbNaZ (Z = Si and Ge) is suggested by the negative estimated magnitudes of formation energies for all compounds, as shown in Table I.

3.2. Elastic properties

To investigate a material's mechanical stability against external forces, it is necessary to calculate its elastic constants C_{ij}. Valuable insights into the mechanical nature of a compound are provided by the values obtained for these constants (stability, stiffness, ductility/brittleness, hardness, etc.). The elastic constants were determined using the IRelast program, incorporated in `Wien2k`, which is specifically designed for cubic systems. The following conditions must be satisfied for the cubic crystal structure to be mechanically stable [35]:

TABLE II. The designed Young's modulus E (GPa), anisotropy factor A, Cauchy's pressure C^P (GPa), Poisson's ratio ν, Pugh's ratio B/G, shear modulus G (GPa), bulk modulus B (GPa), and elastic constants C_{ij} (GPa) for CaRbNaZ (Z = Si and Ge).

Compound	C_{11}	C_{12}	C_{44}	B	G	B/G	ν	C^P	E	A
CaRbNaSi	44.90	10.50	22.31	21.97	20.10	1.09	0.14	-11.81	46.21	1.29
CaRbNaGe	40.24	9.32	22.27	19.63	19.24	1.02	0.13	-12.95	43.51	1.44

$$\begin{aligned} &C_{11} - C_{12} > 0, \\ &C_{11} + 2C_{12} > 0, \\ &C_{44} > 0, \\ &C_{12} < B < C_{11}. \end{aligned} \tag{4}$$

In Table II, using the generalized gradient approximation (GGA), the elastic constants for quaternary CaRbNaZ (Z = Si and Ge) compounds are calculated and demonstrated. The mechanical stability of both compounds in the Type I structure is indicated by our findings, which satisfy the stability conditions. The main mechanical coefficients were examined to explore the hardness of the current materials, such as the Poisson's ratio ν, the ratio B/G, the shear modulus G, Young's modulus E, the Cauchy pressure CP, the Zener anisotropy factor A, and the bulk modulus B, which are also estimated at 0 K and 0 GPa. Applying the Voigt-Reuss-Hill (VRH) approach [36], the mathematical model of the parameters considered in the analysis is represented as follows:

$$B = \frac{C_{11} + 2C_{12}}{3}, \tag{5}$$

$$G_V = \frac{C_{11} - C_{12} + 3C_{44}}{5},$$

$$G_R = \frac{5C_{44}(C_{11} - C_{12})}{4C_{44} + 3(C_{11} - C_{12})}, \tag{6}$$

$$G = \frac{G_V + G_R}{2}, \tag{7}$$

$$CP = C_{12} - C_{44}, \tag{8}$$

$$\nu = \frac{3B - 2G}{2(3B + G)}, \quad A = \frac{2C_{44}}{C_{11} - C_{12}}, \quad E = \frac{9BG}{3B + G}. \tag{9}$$

The obtained bulk modulus B values of 21.97 GPa and 19.63 GPa for CaRbNaSi and CaRbNaGe, respectively, correspond closely to the values derived from the structural properties, as shown in Table II. It is well known that a material is classified as ductile if its Pugh's ratio B/G is 1.75 or higher; otherwise, it is considered brittle [37]. Table II reports the computed B/G values, indicating that both compounds are brittle. A material is deemed brittle if Poisson's ratio ν is less than or equal to 1/3; otherwise, it is considered ductile [38]. The quaternary Heusler alloys (QHAs) CaRbNaZ (Z = Si and Ge) are indicated as brittle, since all computed Poisson's ratios ν in Table II are less than 0.33. The brittleness of these materials can also be analyzed through the calculated negative Cauchy pressure values. Additionally, the Young's modulus value of CaRbNaSi (46.21 GPa) is greater than that of CaRbNaGe (43.51 GPa), which leads to the conclusion that CaRbNaSi is more rigid than CaRbNaGe. Anisotropic characteristics are indicated by a Zener anisotropy factor A value different from unity, signifying the

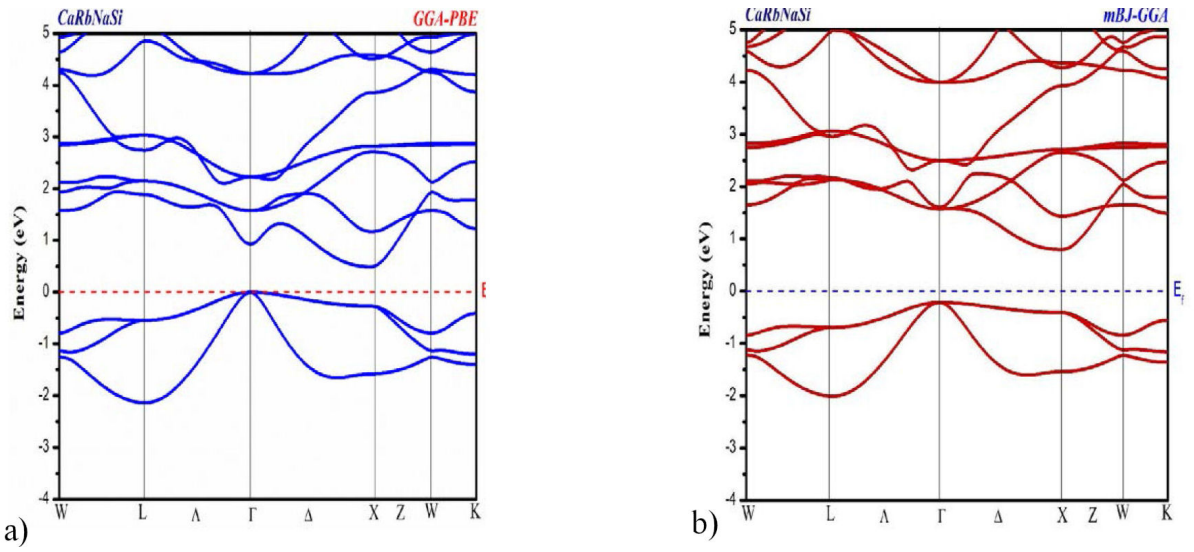

FIGURE 3. Band structure for CaRbNaSi using GGA-PBE and mBJ-GGA.

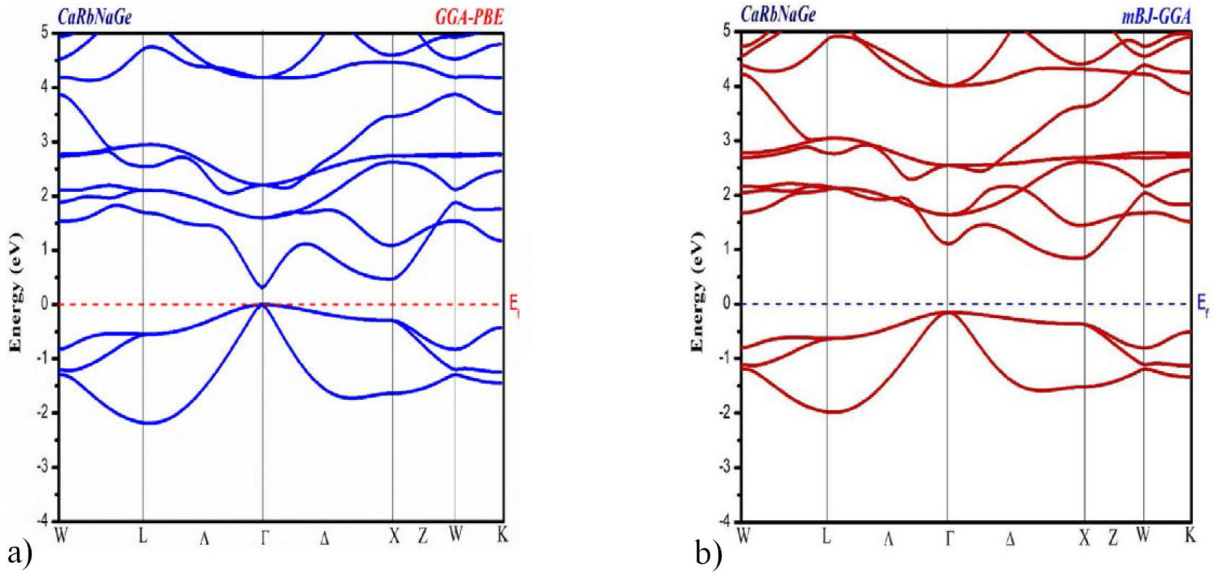

FIGURE 4. Band structure for CaRbNaGe using GGA-PBE and mBJ-GGA.

degree of elastic anisotropy in a crystal. The mechanical anisotropy of these materials is confirmed by the calculated A values, which are 1.29 for CaRbNaSi and 1.44 for CaRbNaGe.

3.3. Electronic properties

3.3.1. Band structure

The resolved band structure along the high symmetry directions $W-L-\Gamma-X-W-K$ in the Brillouin zone (BZ) was computed using the GGA-PBE and GGA-mBJ approximations to investigate the ground state electronic properties of the CaRbNaZ (Z = Si and Ge) quaternary Heusler alloys (QHAs) Figs. 3 and 4. For both approaches, the CaRbNaZ (Z = Si and Ge) alloys are semiconductors. The results indicate that CaRbNaSi has an approximate indirect band gap of 0.49 eV (GGA-PBE) and 1.00 eV (GGA-mBJ) along the $\Gamma-X$ symmetry. In contrast, for CaRbNaGe, along the $\Gamma-\Gamma$ and $\Gamma-X$ symmetries, the material has a direct band gap of about 0.31 eV (GGA-PBE) and an indirect band gap of 0.99 eV (GGA-mBJ) (see Table III). The change in band gap is attributed to the difference in atomic radii of Si and Ge, leading to changes in lattice parameters and orbital overlap. As the lattice constant decreases, the interatomic distance is reduced, resulting in stronger binding forces between the valence electrons and the parent atoms. Consequently, the valence electrons become more tightly bound and require higher energy to become free within the material. Thus, the energy needed for the excitation of valence electrons corresponds to the band gap energy. As a rule of thumb, the band gap is inversely proportional to the interatomic distance [39].

As far as we know, there have been no experimental measurements of the band structure of these compounds available for comparison, while our results indicate that these new materials with narrow-band structures will strongly contribute to improved optical and thermoelectric performance.

3.3.2. Density of states (DOS)

Figures 5 and 6 display the examination of the total and partial densities of states (TDOS and PDOS) for the CaRbNaZ (Z = Si and Ge) compounds to gain a clearer understanding of the electronic contributions responsible for the band structure's characteristics. The semiconducting nature of both materials is demonstrated by the TDOS at the Fermi level being zero, as observed with the GGA and mBJ approximations, which also validates the band structure findings. The states

TABLE III. Band gap calculated using GGA and mBJ-GGA approaches for CaRbNaZ (Z = Si and Ge).

Compound	CaRbNaSi		CaRbNaGe	
	GGA-PBE	mBJ-GGA	GGA-PBE	mBJ-GGA
Band gap (eV)	0.49	1.00	0.31	0.91
Region	Γ-X	Γ-X	Γ-Γ	Γ-X
Type	Indirect	Indirect	Direct	Indirect
Nature	SC	SC	SC	SC

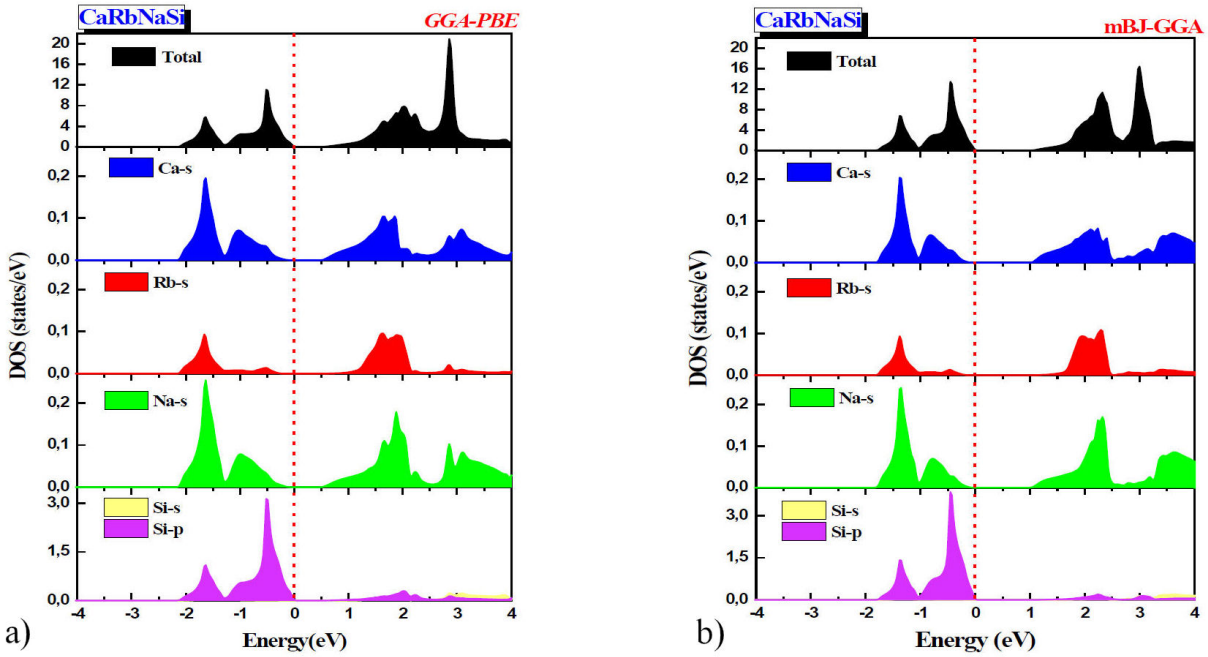

FIGURE 5. The DOS plots of CaRbNaSi under GGA-PBE and mBJ- GGA approximations.

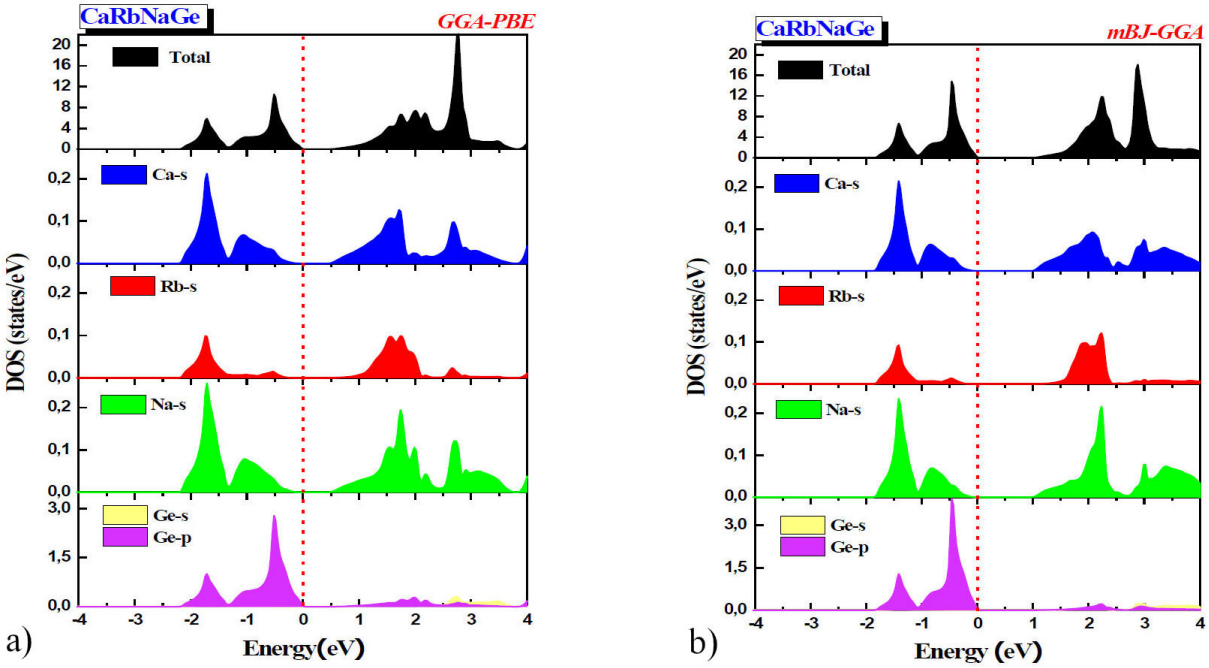

FIGURE 6. The DOS plots of CaRbNaGe under GGA-PBE and mBJ- GGA approximations.

Ca ($4s^2$), Rb ($5s^1$), Na ($3s^1$), Si ($3s^2$, $3p^2$), and Ge ($4s^2$, $4p^2$) are considered as valence electrons. The zero value obtained for the total magnetic moment 0 μ_B using the GGA method verifies the non-magnetic behavior of these compounds according to the Slater-Pauling regime:

$$M_{\text{tot}} = 8 - Z_{\text{tot}}. \tag{10}$$

Here, M_{tot} represents the total magnetic moment, and Z_{tot} denotes the valence electron number, which has a magnitude of 8 for CaRbNaZ (Z = Si and Ge). The region between -2.2 eV and 0 eV in the PDOS is primarily due to 3p-Si states for CaRbNaSi and 4p-Ge states for CaRbNaGe, with minor contributions from Ca-s and Na-s states, as depicted in Fig. 5. Additionally, the region between 0 eV and 4 eV exhibits strong hybridization between Ca-s, Rb-s, and Na-s states, with a weak contribution from 3p-Si and 4p-Ge states in both materials under consideration.

The contribution of Rb states is nearly zero. Therefore, the semiconductor behavior of CaRbNaSi and CaRbNaGe is evident, with the 3p orbitals of Si and the 4p orbitals of Ge primarily influencing their density of states. The optical and transport properties of CaRbNaZ (Z= Si and Ge) QH compounds will be greatly influenced by these alloys.

3.4. Optical properties

To determine a material's response to incident photon energy and its ability to absorb, scatter, and reflect electromagnetic waves, it is crucial to understand its optical properties. For this purpose, the optical performance of cubic CaRbNaZ (Z = Si and Ge) QH compounds is examined in the photon energy range of 0-14 eV, focusing on parameters such as the absorption coefficient, reflectivity, refractive index, and dielectric function utilizing the mBJ-GGA approach [see Fig. 7a)-e)]. The complex dielectric function $\varepsilon(\omega)$ serves as the basis for all the aforementioned optical parameters and is expressed as follows:

$$\varepsilon(\omega) = \varepsilon_1(\omega) + i\varepsilon_2(\omega), \tag{11}$$

where $\varepsilon_1(\omega)$ and $\varepsilon_2(\omega)$ refer to the real and imaginary parts of the dielectric function, respectively. The polarization of light is indicated by the real part of this complex quantity, while the imaginary part reveals details about light absorption. The relationship between $\varepsilon_1(\omega)$ and $\varepsilon_2(\omega)$ is given by the Kramers-Kronig relation [40]:

$$\varepsilon_1(\omega) = 1 + \frac{2}{\pi} P \int_0^{\infty} \frac{\omega' \varepsilon_2(\omega')}{\omega'^2 - \omega^2} d\omega', \tag{12}$$

$$\varepsilon_2(\omega) = \frac{e^2}{\pi m^2 \omega^2} \sum_{v,c} \int_{BZ}^{\infty} |M_{cv}(K)|^2 \times \delta[\omega_{cv}(K) - \omega] d^3K, \tag{13}$$

where P, M, K, h, and ω represent the principal quantum number, molar mass, wave vector, Planck's constant, and angular frequency, respectively. The calculated values of the real and imaginary parts of the dielectric function can be used to derive other optical parameters, including the absorption coefficient $a(\omega)$, reflectivity $R(\omega)$, and refractive index $n(\omega)$ [41–44].

$$a(\omega) = \sqrt{\frac{2\omega}{c}} \left(\sqrt{\varepsilon_1^2(\omega) + \varepsilon_2^2(\omega)} - \varepsilon_1(\omega) \right)^{1/2}, \tag{14}$$

$$R(\omega) = \left| \frac{\sqrt{\varepsilon(\omega)} - 1}{\sqrt{\varepsilon(\omega)} + 1} \right|^2, \tag{15}$$

$$n(\omega) = \left[\frac{\sqrt{\varepsilon_1^2(\omega) + \varepsilon_2^2(\omega)} + \varepsilon_1(\omega)}{2} \right]^{1/2}, \tag{16}$$

Figure 7a) shows the plot of the real part of the dielectric function, $\varepsilon_1(\omega)$. The two resonance peaks at 1.39 eV and 1.45 eV for CaRbNaSi and CaRbNaGe, respectively, correspond to specific light energies where the material is plane-polarized. Furthermore, in the energy range from 2.84 eV to 9 eV, the CaRbNaZ (Z = Si and Ge) quaternary hydrides (QH) demonstrate metallic behavior, as $\varepsilon_1(\omega)$ shows slight negative values. As a result, these compounds have the ability to reflect incident photon radiation in this area. According to Penn's model, $\varepsilon_1(0) \approx 1 + (\hbar\omega_p/E_g)^2$ [45], the static dielectric constant $\varepsilon_1(0)$ at zero frequency ($\omega = 0$) is inversely proportional to the band gap. When Si is replaced with Ge, this constant rises from 10.48 to 11. As shown in Fig. 7b), the imaginary part of the dielectric function $\varepsilon_2(\omega)$ provides information about light absorption. The optimal operational range of the studied QHAs in the visible spectrum is indicated by the highest absorption peaks of $\varepsilon_2(\omega)$ at 2.60 eV for CaRbNaSi and 2.46 eV for CaRbNaGe, making them excellent candidates for optoelectronic applications. Additionally, the optical band gaps of 1.00 eV and 0.91 eV for CaRbNaSi and CaRbNaGe, respectively, closely align with the electronic band gaps calculated from the threshold points of $\varepsilon_2(\omega)$. On the other hand, regarding the absorption coefficient $\alpha(\omega)$, as illustrated in Fig. 7c), it describes the amount of light energy absorbed by the semiconductor and the net absorption edges for incident energy exceeding the band gap. In the visible range, the absorption curve rises rapidly, reaching the greatest magnitude of $90 \times 10^4\,\mathrm{cm}^{-1}$ at 2.95 eV (red), which is higher than the band gap measured from the band structure.

In addition, the maximum absorption attained in the ultraviolet exceeds $10^3 \times 10^4\,\mathrm{cm}^{-1}$ at 6.95 eV, indicating that more transitions occur between the conduction and valence bands. Moreover, the intensity of the peaks in the ultraviolet region is higher than in the visible region, indicating their suitability for optoelectronic devices that operate under UV light.

Figure 7d) depicts the refractive index $n(\omega)$, which indicates the material's transparency and light dispersion properties. If $n(0)$ is around zero, the material is transparent, while positive values measure light absorption. The plot indicates that the behavior of the refractive index mirrors that of the real part of the dielectric function $\varepsilon_1(\omega)$. The static values of the refractive index $n(0)$, which are equal to 3.24 and 3.34 for CaRbNaSi and CaRbNaGe, respectively, are in accordance with the relation $n(0) = \sqrt{\varepsilon_1(0)}$.

Additionally, the refractive index continues to increase across the energy span of $[0 - 14]$ eV, attributed to the linear response of CaRbNaZ (Z = Si and Ge) to light frequency [46]. A significant portion of the light in the infrared (IR) and visible regions contributes substantially to the electronic transition. In the UV spectrum, within the 6 to 13 eV energy range, the compound exhibits superluminal properties as the refractive index ($n = c/v$) drops below one. This indicates that the velocity of the incident radiation v is greater than the speed of light in a vacuum c [47, 48].

The response of the present materials under incident photon radiation is also studied by calculating the reflectivity $R(\omega)$, which illustrates the ratio between the reflected energy and the total incident energy, as shown in Fig. 7e). Its values

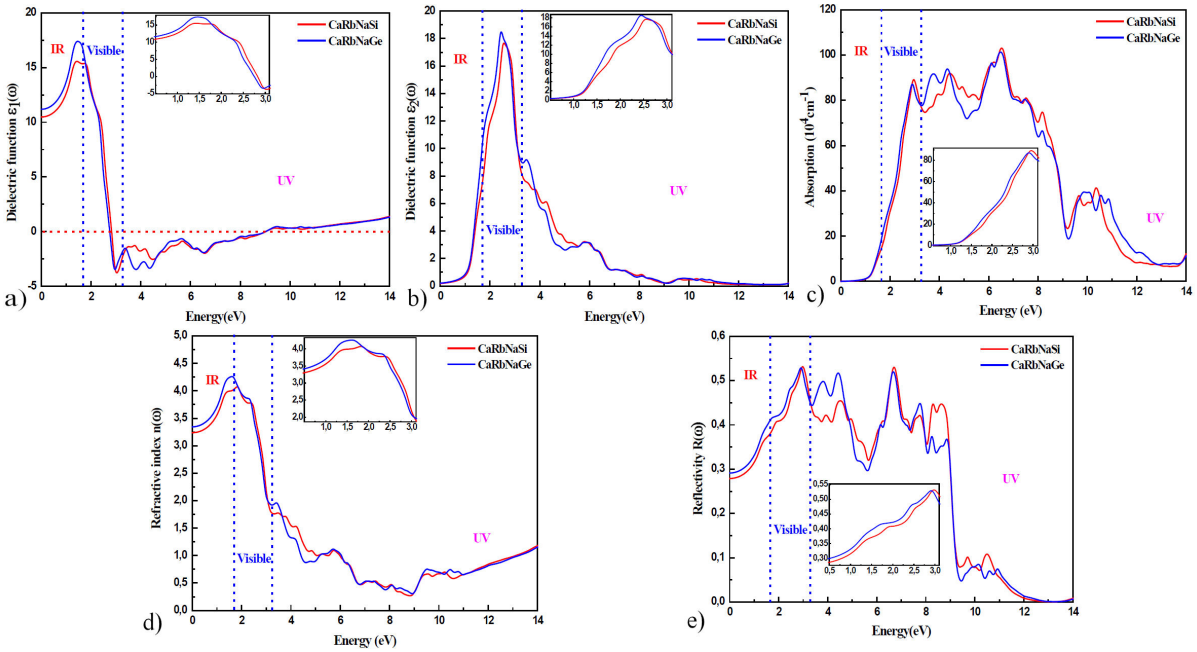

FIGURE 7. Computed results for a), b) real and imaginary parts of dielectric function, c) absorption coefficient, d) refractive index, and e) reflectivity of CaRbNaZ (Z= Si and Ge).

increase from the zero edge $R(0)$ and reach maximum values of 53% in the visible and UV ranges, where absorption is lowest, as shown in Fig. 7c). The high reflectivity values of these materials suggest their potential use as reflectors in optical devices. The reflection of light photons at varying angles on the surfaces of the two materials causes differences in peak intensity.

3.5. Thermoelectric properties

Utilizing semi-classical Boltzmann transport theories in the BoltzTraP code [49], we examined various transport coefficients of CaRbNaSi and CaRbNaGe alloys in terms of electrical conductivity σ/τ, Seebeck coefficient S, electronic contribution of thermal conductivity κ_e/τ, and the figure of merit ZT. Through the mBJ-GGA approximation, we drew the variants of these coefficients for a temperature range of 200 - 1000 K close to the Fermi level.

3.5.1. Seebeck coefficient

The Seebeck effect of matter describes how electricity is created between a thermocouple when subjected to a temperature gradient at the ends. The movement of charge carriers, induced by this temperature gradient, results in the creation of an electric current [50]. A high Seebeck coefficient is essential for an efficient thermoelectric device.

Figure 8 demonstrates the Seebeck coefficient (S) as a function of temperature, derived from the given expression [51, 52]:

$$S = \frac{\Delta V}{\Delta T}. \tag{17}$$

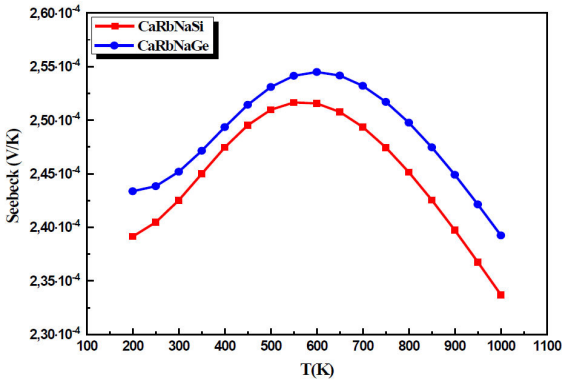

FIGURE 8. Seebeck coefficient versus temperature for CaRbNaZ (Z= Si and Ge).

The Seebeck coefficient for both composites is positive $S > 0$, clearly indicating their p-type semiconductor nature [53, 54]. Additionally, the highest Seebeck coefficient values for both compounds are observed at 600 K, with CaRbNaSi reaching around 252 μV/K and CaRbNaGe achieving approximately 254 μV/K. This sharp increase in the density of states around the Fermi level results in high Seebeck coefficients, which is a crucial factor for the efficient performance of thermoelectric materials [55]. For both compounds, beyond the temperature of 600 K, the Seebeck coefficient S decreases as the temperature continues to rise.

3.5.2. Electrical conductivity

The relationship between electrical conductivity data σ/τ per relaxation time and temperature is shown in Fig. 9. As temperature rises, electrical conductivity increases, which cor-

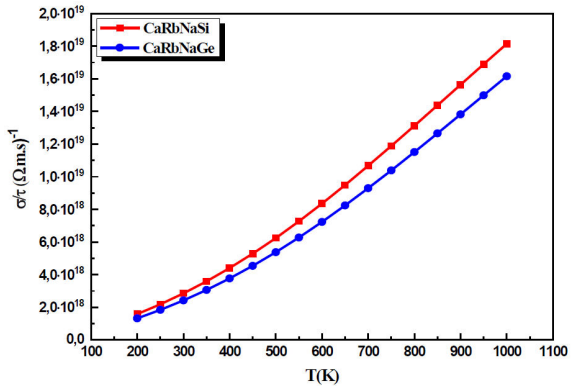

FIGURE 9. Electrical conductivity versus temperature for CaRbNaZ (Z= Si and Ge).

responds with the semiconducting behavior indicated by the band structure and total density of states (TDOS). The values of σ/τ attain maximum values of 1.81×10^{19} and 1.61×10^{19} ω·m·s^{-1} for CaRbNaSi and CaRbNaGe, respectively, at 1000 K. At elevated temperatures, more electrons are generated due to bond breaking, and these electrons possess higher kinetic energy. Primarily attributed to their intrinsically narrow-band gaps, these increases justify the suitability of these alloys for thermoelectric applications such as cooling, heating, and power generation.

3.5.3. *Thermal conductivity*

The equation $K = K_e + K_{ph}$ captures the thermal conductivity, which arises from two distinct contributions: the thermal conductivity due to electrons K_e and the thermal conductivity due to phonons K_{ph}. This dual contribution underscores the comprehensive nature of thermal conductivity, highlighting the significant roles of electrons and phonons in the heat conduction process. The thermal conductivity due to free carriers constitutes the electronic part, whereas the temperature rise induces lattice vibrations, contributing to the phononic component [56].

This distinction highlights how both lattice dynamics and free carrier movement play pivotal roles in overall thermal conductivity. Due to the limitations of the classical theory-based BoltzTraP code [57], the phononic contribution was excluded, and only the electronic component was calculated in our present results. Figure 10 illustrates the variation of the electronic component of thermal conductivity K_ϵ/τ with temperature. The quasi-linear profile reveals that K_ϵ/τ increases with rising temperature for both compounds. This similarity is clearly reflected in the plots for both electrical and electronic thermal conductivity. The findings are aligned with the Wiedemann-Franz law:

$$K_\epsilon = L\sigma T$$

where $L = 2.44 \times 10^{-8}\,\mathrm{W}\cdot\Omega\cdot\mathrm{K}^{-2}$ and denotes the Lorenz number, σ is the electrical conductivity, and T is the absolute temperature, correspondingly [58]. At room temperature, the thermal conductivity values are approximately 6.76×10^{13} W/m·K·s for CaRbNaSi and 5.83×10^{13} W/m·K·s for CaRbNaGe.

3.5.4. *Figure of Merit*

A figure of merit (ZT) near or above one indicates that a material is highly effective for use in thermoelectric devices [59]. Figure 11 shows the variation of ZT with temperature. For both compounds, ZT remains relatively consistent across the temperature range of 200 K to 1000 K, fluctuating between 0.77 and 0.82 for CaRbNaSi, and between 0.82 and 0.86 for CaRbNaGe. At ambient temperature (300 K), the p-type dimensionless figure of merit for these materials is found to be 0.76 and 0.80 for CaRbNaSi and CaRbNaGe, respectively.

In general, ZT magnitudes are considerably higher than those described in published research for QHAs like CoFeXSn (X=Ru, Zr, Hf, Ta) (0.04 - 0.14) [60], FeCrYSn (Y=Ti, Hf) (0.47, 0.61), FeCrYSb (Y=Ti, Zr, Hf) (0.55, 0.11, 0.13) [61], LaCoCrGa (0.40) [62], and CoRhMnAs (0.50) [63]. The obtained merit factor values confirm that CaRbNaZ (Z=Si and Ge) may be used as alternative green energy resources.

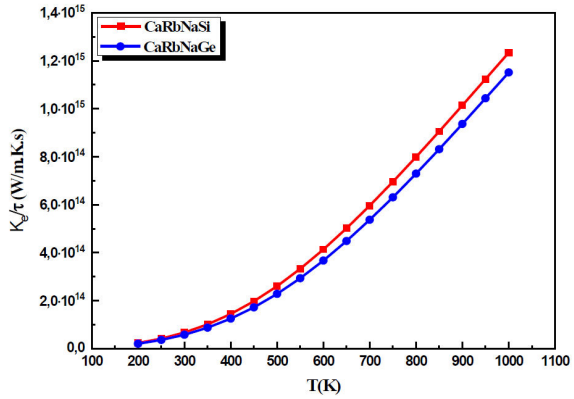

FIGURE 10. Electronic thermal conductivity versus temperature for CaRbNaZ (Z= Si and Ge).

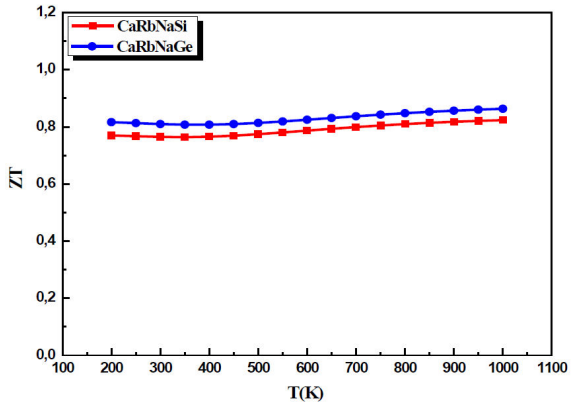

FIGURE 11. Figure of merit ZT versus temperature for CaRbNaZ (Z= Si and Ge).

4. Conclusion

In the present paper, a comprehensive analysis of the thermoelectric, optical, elastic, electronic, and structural characteristics of CaRbNaZ (Z = Si, Ge) compounds has been conducted using Density Functional Theory (DFT) and Boltzmann transport theory. The negative values of the calculated formation and cohesive energies indicate that these alloys possess good chemical stability. Both compounds are non-magnetic (NM) semiconductors with narrow-band gaps, ranging from 0.49 to 1.00 eV, as revealed by the assessment of their band structure.

According to the Partial Density of States (PDOS) plots, the p-orbitals of the main group elements (Si and Ge) are the major contributors to the density of states. The acquired elastic parameters allow us to conclude that these compounds are mechanically stable in a cubic phase and exhibit brittle behavior.

Due to their high suitability for producing solar cells and optical devices, the quaternary Heusler alloys under examination demonstrate an outstanding absorption capability in the visible and ultraviolet regions of the light spectrum. Furthermore, both materials show improved thermoelectric performance in the temperature range of 200 - 1000 K using the BoltzTraP code. At ambient temperature, the p-type figure of merit values are found to be 0.76 and 0.80 for CaRbNaSi and CaRbNaGe, respectively, suggesting that both compounds are excellent contenders for thermoelectric device applications.

This exceptional absorption capability in the visible and ultraviolet regions of the light spectrum could pave the way for experimental research on quaternary Heusler compounds CaRbNaZ (Z = Si, Ge) semiconductors, particularly in the production of solar cells and optical devices.

Declaration of competing interest

The authors declare that they have no known competing financial interests or personal relationships that could have appeared to influence the work reported in this paper.

1. X. Zhang, L.-D. Zhao, Thermoelectric materials: Energy conversion between heat and electricity, *J. Mater.* **1** (2015) 92. https://doi.org/10.1016/j.jmat.2015.01.001
2. B.I. Ismail, W.H. Ahmed, Thermoelectric Power Generation Using Waste-Heat Energy as an Alternative Green Technology, *Recent Pat. Electr. Eng.* **2** (2009) 27. https://doi.org/10.2174/1874476110902010027
3. B.G. Levi, Simple compound manifests record-high thermoelectric performance, *Phys. Today* **67** (2014) 14. https://doi.org/10.1063/PT.3.2404
4. A.D. LaLonde, Y. Pei, H. Wang, G.J. Snyder, Lead telluride alloy thermoelectrics, *Mater. Today* **14** (2011) 526. https://doi.org/10.1016/S1369-7021(11)70278-4
5. S. Yousuf, D.C. Gupta, Investigation of electronic, magnetic and thermoelectric properties of Zr_2NiZ (Z = Al, Ga) ferromagnets, *Mat. Chem. Phys.* **192** (2017) 33. https://doi.org/10.1016/j.matchemphys.2017.01.056
6. H. Lamkaouane *et al*., Investigation of the different possible energy band structure configurations for planar heterojunction organic solar cells, *Solid-State Electron.* **191** (2022) 108254. https://doi.org/10.1016/j.sse.2022.108254
7. J.W.G. Bos, R.A. Downie, Half-Heusler thermoelectrics: a complex class of materials, *J. Phys. Condens. Matter* **26** (2014) 433201. https://doi.org/10.1088/0953-8984/26/43/433201
8. H. Kara, M.U. Kahaly, K. Özdoğan, Thermoelectric response of quaternary Heusler compound CrVNbZn, *J. Alloys Compd.* **735** (2018) 950. https://doi.org/10.1016/j.jallcom.2017.11.022
9. A. Berche and P. Jund, Oxidation of half-Heusler NiTiSn materials: Implications for thermoelectric applications, *Intermetallics* **92** (2018) 62. https://doi.org/10.1016/j.intermet.2017.09.014
10. X. Dai *et al*., New quaternary half metallic material CoFeMnSi, *J. Appl. Phys.* **105** (2009) 07E901. https://doi.org/10.1063/1.3062812
11. Q. Gao, I. Opahle, H. Zhang, High-throughput screening for spin-gapless semiconductors in quaternary Heusler compounds, *Phys. Rev. Materials* **3** (2019) 024410. https://doi.org/10.1103/PhysRevMaterials.3.024410
12. C.K. Barman, C. Mondal, B. Pathak, A. Alam, Quaternary Heusler alloy: An ideal platform to realize triple point fermions, *Phys. Rev. B* **99** (2019) 045144. https://doi.org/10.1103/PhysRevB.99.045144
13. J. He, S.S. Naghavi, V.I. Hegde, M. Amsler, C. Wolverton, Designing and discovering a new family of semiconducting quaternary Heusler compounds based on the 18-Electron Rule, *Chem. Mater.* **30** (2018) 4978. https://doi.org/10.1021/acs.chemmater.8b01096
14. T. Roy, M. Tsujikawa, T. Kanemura, M. Shirai, Ab-initio study of electronic and magnetic properties of CoIrMnZ (Z = Al, Si, Ga, Ge) Heusler alloys, *J. Magn. Magn. Mater.* **498** (2020) 166092. https://doi.org/10.1016/j.jmmm.2019.166092
15. Y. Han, Y. Wu, T. Li, R. Khenata, T. Yang, X. Wang, Electronic, Magnetic, Half-Metallic, and Mechanical Properties of a New Equiatomic Quaternary Heusler Compound YRhTiGe: A First-Principles Study, *Materials* **11(5)** (2018) 797. https://doi.org/10.3390/ma11050797
16. L. Feng, J. Ma, Y. Yang, T. Lin, L. Wang, The Electronic, Magnetic, Half-Metallic, and Mechanical Properties of the Equiatomic Quaternary Heusler Compounds FeRhCrSi and FePdCrSi: A First-Principles Study, *Appl. Sci.* **8(12)** (2018) 2370. https://doi.org/10.3390/app8122370

17. H. Moujri, M. Berber, M. Mebrek, A. Boudali, T. Ouahrani, Structural, elastic, electronic, and magnetic properties of new quaternary Heusler alloy PdCoMnGa and PdCoMnAl, *Indian J. Phys.* **96** (2022) 1025. https://doi.org/10.1007/s12648-021-02024-1

18. S. Alsayegh, H. Alqurashi, E. Andharih, B. Hamad, M.O. Manasreh, First-principles investigations of the electronic, magnetic, and thermoelectric properties of CrTiRhAl quaternary Heusler alloy, *J. Magn. Magn. Mater.* **568** (2023) 170421. https://doi.org/10.1016/j.jmmm.2023.170421

19. Y. Gupta, M.M. Sinha, S.S. Verma, Exploring the structural, elastic, lattice dynamical stability and thermoelectric properties of semiconducting novel quaternary Heusler alloy LiScPdPb, *J. Solid State Chem.* **304** (2021) 122601. https://doi.org/10.1016/j.jssc.2021.122601

20. T.T. Lin, Q. Gao, G.D. Liu, X.F. Dai, X.M. Zhang, H.B. Zhang, Dynamical stability, electronic and thermoelectric properties of quaternary ZnFeTiSi Heusler compound, *Curr. Appl. Phys.* **19** (2019) 721. https://doi.org/10.1016/j.cap.2019.03.020

21. P. Blaha, K. Schwarz, G.K.H. Madsen, D. Kvasnicka, J. Luitz, WIEN2k, Efficient linearization of the augmented plane-wave method, Vienna (2001).

22. J.P. Perdew, K. Burke, M. Ernzerhof, Generalized Gradient Approximation Made Simple, *Phys. Rev. Lett.* **77** (1996) 3865. https://doi.org/10.1103/PhysRevLett.77.3865

23. A. Radzwan, R. Ahmed, A. Shaari, Y.X. Ng, A. Lawal, First-principles calculations of the stibnite at the level of modified Becke-Johnson exchange potential, *Chin. J. Phys.* **56** (2018) 1331. https://doi.org/10.1016/j.cjph.2018.03.005

24. M. Manzoor *et al*., First-principles calculations to investigate structural, electronic, optical and thermoelectric properties of novel double perovskite Cs_2CeAgX_6 (X = Cl, Br) for optoelectronic and thermoelectric applications, *Chem. Phys.* **575** (2023) 112065. https://doi.org/10.1016/j.chemphys.2023.112065

25. Y.S. Kim, M. Marsman, G. Kresse, F. Tran, and P. Blaha, Towards efficient band structure and effective mass calculations for III-V direct band-gap semiconductors, *Phys. Rev. B* **82** (2010) 205212. https://doi.org/10.1103/PhysRevB.82.205212

26. D. Abdullah and D.C. Gupta, Scrutinizing the structural, optoelectronic, mechanical, and thermoelectric properties of semiconductor lead-free double perovskites $A_2AgMoBr_6$ (A = K, Rb, Cs), *Opt. Quantum Electron.* **55** (2023) 1277. https://doi.org/10.1007/s11082-023-05493-2

27. G. Rehman, M. Shafiq, Saifullah, R. Ahmad, S. Jalali-Asadabadi, M. Maqbool, I. Khan, H. Rahnamaye-Aliabad, I. Ahmad, Electronic Band Structures of the Highly Desirable III-V Semiconductors: TB-mBJ DFT Studies, *J. Electron. Mater.* **45** (2016) 3314. https://doi.org/10.1007/s11664-016-4492-7

28. J. A. Camargo-Martínez and R. Baquero, Performance of the modified Becke-Johnson potential for semiconductors, *Phys. Rev. B* **86** (2012) 195106. https://doi.org/10.1103/PhysRevB.86.195106

29. G.K.H. Madsen, J. Carrete, M.J. Verstraete, BoltzTraP2, a program for interpolating band structures and calculating semi-classical transport coefficients, *Comput. Phys. Commun.* **231** (2018) 140. https://doi.org/10.1016/j.cpc.2018.05.010

30. S. Idrissi, H. Labrim, S. Ziti, L. Bahmad, Investigation of the physical properties of the equiatomic quaternary Heusler alloy CoYCrZ (Z = Si and Ge): a DFT study, *Appl. Phys. A* **126** (2020) 190. https://doi.org/10.1007/s00339-020-3354-6

31. F. Bendahma, M. Mana, S. Terkhi, S. Cherid, B. Bestani, S. Bentata, Investigation of high figure of merit in semiconductor XHfGe (X = Ni and Pd) half-Heusler alloys: Ab-initio study, *Comput. Cond. Matter* **21** (2019) e00407. https://doi.org/10.1016/j.cocom.2019.e00407

32. Y. Li, J. Zhu, R. Paudel, J. Huang, F. Zhou, Ab initio predictions of stability, half-metallicity and magnetism in Co_2NbAl and Co_2ZrAl full-Heusler alloys, *Vacuum* **192** (2021) 110418. https://doi.org/10.1016/j.vacuum.2021.110418

33. G. Srivastava, D. Weaire, The theory of the cohesive energies of solids, *Adv. Phys.* **36** (1987) 463. https://doi.org/10.1080/00018738700101042

34. J. Du, L. Feng, X. Wang, Z. Qin, Z. Cheng, L. Wang, Novel bipolar magnetic semiconducting and fully compensated ferrimagnetic semiconducting characters in newly designed LiMgPdSn-type compounds: KCaCX (X = O, S, and Se), *J. Alloys Compd.* **710** (2017) 1. https://doi.org/10.1016/j.jallcom.2017.03.262

35. J.H. Wang, S. Yip, S.R. Phillpot, D. Wolf, Crystal instabilities at finite strain, *Phys. Rev. Lett.* **71** (1993) 4182. https://doi.org/10.1103/PhysRevLett.71.4182

36. R. Hill, The Elastic Behaviour of a Crystalline Aggregate, *Proc. Phys. Soc. A* **65** (1952) 349. https://doi.org/10.1088/0370-1298/65/5/307

37. S. F. Pugh, Relations between the elastic moduli and the plastic properties of polycrystalline pure metals, *Lond. Edinb. Dubl. Phil. Mag.* **45** (1954) 823, https://doi.org/10.1080/14786440808520496

38. I.N. Frantsevich, F.F. Voronov, S.A. Bokuta, Handbook on Elastic Constants and Moduli of Elasticity for Metals and Nonmetals (Naukova Dumka, Kiev, 1982).

39. B. J. Abdullah, Size effect of band gap in semiconductor nanocrystals and nanostructures from density functional theory within HSE06, *Mat. Sci. Semicon. Proc.* **137** (2022) 106214, https://doi.org/10.1016/j.mssp.2021.106214

40. M. Grundmann, Kramers-Kronig Relations, In The Physics of Semiconductors: An Introduction Including Nanophysics and Applications (Springer Berlin Heidelberg, Berlin, Heidelberg, 2010) pp. 775-776, https://doi.org/10.1007/978-3-642-13884-326.

41. M. Irfan *et al*., Electronic structure and optical properties of TaNO: An ab initio study, *J. Mol. Graph. Model.* **92** (2019) 296, https://doi.org/10.1016/j.jmgm.2019.08.006

42. K. Yamamoto, H. Ishida, Kramers-Kronig analysis applied to reflection-absorption spectroscopy, *Vib. Spectrosc.* **15** (1997) 27. https://doi.org/10.1016/S0924-2031(97)00017-9

43. H.C. Kandpal, G.H. Fecher, C. Felser, Calculated electronic and magnetic properties of the half-metallic, transition metal based Heusler compounds, *J. Phys. D Appl. Phys.* **40** (2007) 1507. https://doi.org/10.1088/0022-3727/40/6/S01

44. M. L. Cohen, J. R. Chelikowsky, Wurtzite Structure Semiconductors, In Electronic Structure and Optical Properties of Semiconductors (Springer Berlin Heidelberg, Berlin, Heidelberg, 1989) pp. 140-160, https://doi.org/10.1007/978-3-642-61338-8_9

45. D. Penn, Wave-Number-Dependent Dielectric Function of Semiconductors, *Phys. Rev.* **128** (1962) 2093. https://doi.org/10.1103/PhysRev.128.2093

46. N. Yaqoob, B. Sabir, G. Murtaza, R.M. Arif Khalil, N. Muhammad, A. Laref, Structural, electronic, magnetic, optical and thermoelectric response of half-metallic $AMnTe_2$ (A = Li, Na, K): An ab-initio calculations, *Physica B: Condens. Matter* **574** (2019) 311656. https://doi.org/10.1016/j.physb.2019.08.033

47. L.J. Wang, A. Kuzmich, A. Dogariu, Gain-assisted superluminal light propagation, *Nature* **406** (2000) 277. https://doi.org/10.1038/35018520

48. M.A. Ali, N. Alam, Meena, S. Ali, S.A. Dar, A. Khan, G. Murtaza, A. Laref, A theoretical study of the structural, thermoelectric, and spin-orbit coupling influenced optoelectronic properties of $CsTmCl_3$ halide perovskite, *Int. J. Quant. Chem.* **120** (2020) e26141. https://doi.org/10.1002/qua.26141

49. G.K. Madsen, D.J. Singh, BoltzTraP. A code for calculating band-structure dependent quantities, *Comput. Phys. Commun.* **175** (2006) 67. https://doi.org/10.1016/j.cpc.2006.03.007

50. S. Sâad Essaoud, A.S. Jbara, First-principles calculation of magnetic, structural, dynamic, electronic, elastic, thermodynamic and thermoelectric properties of Co_2ZrZ (Z = Al, Si) Heusler alloys, *J. Magn. Magn. Mater.* **531** (2021) 167984. https://doi.org/10.1016/j.jmmm.2021.167984

51. O. Rabina, Y.M. Lin, M.S. Dresselhaus, Anomalously high thermoelectric figure of merit in $Bi_{1-x}Sb_x$ nanowires by carrier pocket alignment, *Appl. Phys. Lett.* **79** (2001) 81. https://doi.org/10.1063/1.1379365

52. T. Takeuchi, Conditions of Electronic Structure to Obtain Large Dimensionless Figure of Merit for Developing Practical Thermoelectric Materials, *Mater. Trans.* **50** (2009) 2359. https://doi.org/10.2320/matertrans.M2009143

53. N. J. Jeon, J. H. Noh, Y.C. Kim, W.S. Yang, S. Ryu, S.I. Seok, Solvent engineering for high-performance inorganic-organic hybrid perovskite solar cells, *Nat. Mater.* **13** (2014) 897. https://doi.org/10.1038/nmat4014

54. D. Zhou, T. Zhou, Y. Tian, X. Zhu, Y. Tu, Perovskite-Based Solar Cells: Materials, Methods, and Future Perspectives, *J. Nanomater.* **2018** (2018) 1. https://doi.org/10.1155/2018/8148072

55. D.I. Bilc, G. Hautier, D. Waroquiers, G.-M. Rignanese, P. Ghosez, Low-Dimensional Transport and Large Thermoelectric Power Factors in Bulk Semiconductors by Band Engineering of Highly Directional Electronic States, *Phys. Rev. Lett.* **114** (2015) 136601. https://doi.org/10.1103/PhysRevLett.114.136601

56. J. He et al., Ultralow Thermal Conductivity in Full Heusler Semiconductors, *Phys. Rev. Lett.* **117** (2016) 046602. https://doi.org/10.1103/PhysRevLett.117.046602

57. M. Hammou, F. Bendahma, M. Mana, S. Terkhi, N. Benderdouche, Z. Aziz, B. Bouhafs, Thermoelectric and Half-Metallic Behavior of the Novel Heusler Alloy RbCrC: Ab initio DFT Study, *SPIN* **10** (2020) 2050029, https://doi.org/10.1142/S2010324720500290.

58. S. Ahmad, S.D. Mahanti, Energy and temperature dependence of relaxation time and Wiedemann-Franz law on PbTe, *Phys. Rev. B* **81** (2010) 165203. https://doi.org/10.1103/PhysRevB.81.165203

59. K. Kaur, R. Kumar, D.P. Rai, A promising thermoelectric response of HfRhSb half-Heusler compound at high temperature: A first-principle study, *J. Alloys Compd.* **763** (2018) 1018, https://doi.org/10.1016/j.jallcom.2018.06.034

60. Ab. Quyoom Seh, Dinesh C. Gupta, Quaternary Heusler alloys: A future perspective for revolutionizing conventional semiconductor technology, *J. Alloys Compd.* **871** (2021) 159560. https://doi.org/10.1016/j.jallcom.2021.159560

61. R. Prakash, G. Kalpana, First-principles study on novel Fe-based quaternary Heusler alloys, with robust half-metallic, thermoelectric and optical properties, *RSC Adv.* **13** (2023) 10847. https://doi.org/10.1039/D3RA00942D

62. S. Singh, Dinesh C. Gupta, Lanthanum based quaternary Heusler alloys LaCoCrX (X = Al, Ga): Hunt for half-metallicity and high thermoelectric efficiency, *Results Phys.* **13** (2019) 102300. https://doi.org/10.1016/j.rinp.2019.102300

63. Ab. Quyoom Seh, Dinesh C. Gupta, Exploration of highly correlated Co-based quaternary Heusler alloys for spintronics and thermoelectric applications, *Int. J. Energy Res.* **43** (2019) 8864. https://doi.org/10.1002/er.4853